

Research Article

The barotropic simulation of coastal current in Soc Trang derived from a hydraulic model in curvilinear coordinates

Kim Tran Thi¹, Huy Dinh Ngoc¹, Huy Nguyen Dam Quoc², Phuoc Nguyen Van³,
Phung Nguyen Ky¹, and Bay Nguyen Thi^{4,5*}

¹ Faculty of Marine Resource Management, Ho Chi Minh City University of Natural Resources and Environment, Vietnam; tkim@hcmunre.edu.vn; kyphungng@gmail.com; huyspb@gmail.com

² Institute of Coastal and Offshore Engineering, Vietnam, 658 Vo Van Kiet, Ward 1, District 5, Ho Chi Minh City, Vietnam; damquochuy71@gmail.com

³ Ho Chi Minh City Union of Science and Technology Associations, 224 Dien Bien Phu, Ward 7, District 3, Ho Chi Minh City Vietnam; nvphuoc196@gmail.com

⁴ Department of Fluid Mechanics, Ho Chi Minh City University of Technology, Vietnam, 268 Ly Thuong Kiet Street, Ward 14, District 10, Ho Chi Minh City, Vietnam; ntbay@hcmut.edu.vn

⁵ Vietnam National University Ho Chi Minh City, Vietnam, Linh Trung Ward, Thu Duc District, Ho Chi Minh City, Vietnam; ntbay@hcmut.edu.vn

*Corresponding author: ntbay@hcmut.edu.vn; Tel.: +84-902698585

Received: 18 April 2023; Accepted: 26 June 2023; Published: 25 September 2023

Abstract: The coastal current plays a vital role in the transportation of sediment near the shoreline, significantly impacting the distribution of sediment grain sizes and shoreline transformations. This study focuses on examining the near-shore coastal current along the Soc Trang Province coast in Vietnam, considering the combined influences of waves, winds, and tides by utilizing a model in curvilinear coordinate system. Rigorous calibration and validation of the model are conducted using data obtained from measurement stations, revealing a consistent correlation between the observed data and simulated results. The direction of the coastal current, governed by the interplay of waves and winds, exhibits variation according to the monsoon season. During the northeast monsoon, the flow velocity is notably influenced, surpassing the impact of the southwest monsoon. In the northeast monsoon season, the tidal currents from the northeast to southwest align with the wave-induced current, resulting in an amplified coastal current during both spring tide (3-5%) and neap tide (2-5%). Conversely, in the southwest monsoon season, the tidal currents and wave-induced current move in opposing directions, leading to a reduction in coastal current velocities during high tide (3-4%) and low tide (3-4.5%). On the other hand, the impact of wind-induced current is negligible due to the small and low-lying nature of these areas, thereby minimizing the influence of wind on the overall flow dynamics.

Keywords: Coastal current; Hydraulic model; Tidal current; Wave induced current; Wind induced current.

1. Introduction

The near-shore estuary and coastal environment exhibit intricate natural processes influenced by tides, waves, currents, saline water, and their interplay. Investigating the coastal current within such areas serves as a foundational step for future studies involving

sediment transport, shoreline accretion and erosion, coastal protection strategies, port and harbor design, navigation, flood prediction, coastal erosion mitigation, and changes in the continental shelf seabed. By understanding the dynamics of coastal currents, we gain valuable insights into the complex mechanisms shaping these environments, enabling us to make informed decisions and develop effective solutions for coastal management and sustainable development [1–2]. Furthermore, the coastal current significantly influences the process of saline intrusion, particularly in the context of climate change and rising sea levels [3]. As the current is influenced by a combination of factors including waves, wind, and tides, many studies on coastal currents tend to concentrate on examining one of these factors individually.

In recent years, hydraulic models like TELEMAC have been extensively utilized for studying hydraulic features in rivers, estuaries, coastal areas, and oceans [4–5]. Numerical simulations using these models have proven to be highly valuable and cost-effective tools for enhancing our understanding of these phenomena. Research in this field often involves the use of shallow water equations (SWE) or the application of the finite-volume primitive equation Community Ocean Model (FVCOM) [6]. The SWE, initially proposed by Saint-Venant in 1871 to simulate flow in open channels [7–8], has been widely employed for describing shallow water flows. It can be derived as a simplification of the Navier–Stokes equation through vertical dimension averaging [9]. Two-dimensional numerical models commonly used for near-shore hydrodynamics include the CCHE2D hydraulic model, developed by Jia and Wang in 1999 [10]; However, the shear stress terms at the water surface were not considered in the 2001 version of this model [11]. The CCHE2D model, created by Mississippi State University, aims to simulate hydraulic transmission, water quality, sediment transport, and riverbed fluctuations [12]. Another notable model is TELEMAC, developed in 1987 by the French National Hydraulic and Environment Laboratory (<http://www.opentelemac.org/>). TELEMAC is a powerful integrated modeling tool capable of handling 1D, 2D, and 3D flows. The model employs flexible meshing and finite-element numerical schemes. Modules such as TELEMAC2D/3D and SISYPHE are used to simulate flow, sediment transport, and bottom evolution [5]. A widely used commercial software, MIKE 21, was developed by the Danish Hydraulic Institute (DHI) for simulating various flow features in creeks, rivers, lakes, estuaries, bays, and coastal areas [13]. The software comes in two versions: classic and flexible mesh (FM). The FM version utilizes a triangulated and unstructured mesh, offering improved resolution within the study domain [14]. Moreover, the MIKE 21C model employs curvilinear finite difference grids to predict hydraulic and morphological changes in two dimensions, optimizing results near land boundaries [15]. Most current modeling approaches employ structured curvilinear systems or unstructured triangular assemblies for mesh generation. While the unstructured approach provides greater flexibility in shape, the resulting model outputs may be less accurate due to the stretching of triangular grid cells in the current direction [16–17]. In contrast, curvilinear grid cells provide more accurate model outputs by closely aligning with land boundaries, especially in areas with complex bathymetry. When curvilinear coordinates are used, the velocity in the ξ direction (a coordinate direction in the curvilinear system) resulting from complex bathymetry is fully accounted for within the model through the Cartesian coordinate system. Hence, simulation results based on curvilinear coordinates tend to be superior to those based on the Cartesian coordinate system in areas with complex bathymetry [18–20].

Soc Trang, a coastal province located in the Mekong Delta, covers an area of 3311.87 km² and is home to approximately 1.3 million residents. Situated in the estuary region of the Hau River, a major tributary of the Mekong River, the northeastern part of the province is bounded by the Hau River, while the southeastern region is adjacent to the sea [21]. The study area experiences a tropical monsoon climate characterized by two distinct seasons:

the flood season (May to October) and the drought season (November to April). River flow and tidal currents exert a significant influence on the area, with the tides being of mixed semidiurnal and diurnal nature and displaying pronounced diurnal inequality [22–23]. The Tra Vinh - Soc Trang coast in the Mekong Delta is characterized by the presence of a tidal beach with multiple intertidal bars, shaped by the interaction of waves and tides [24]. While the coastal current in Soc Trang Province is only minimally influenced by wind-affected and wave-induced currents, these factors play a crucial role in shaping sediment transport patterns and the geomorphological evolution of the coastline [24]. Hydraulic processes at the river mouths are heavily influenced by both river discharges and monsoons [24–25]. The study of [25] has demonstrated that the direction of suspended sediment movement depends on the prevailing monsoon direction. The coastal estuarine area in the Mekong Delta has undergone complex changes in its hydraulic regime due to climate change and upstream development [26]. The coast of Soc Trang has been extensively studied regarding the contribution of natural hydrodynamic sediment redistribution and erosion caused by human activities [25, 27–30]. Notably, a three-dimensional hydrodynamic redistribution model has been proposed to account for sediment movement from land, rivers, and other sources. This model incorporates calibration based on a combination of observations, laboratory experiments, and satellite analysis. The study by [27] provides a brief illustration of wind-induced and wave-induced currents in the area. However, in-depth studies on the impacts of factors such as waves, wind, and tides on coastal current are still limited. With the strong occurrence of erosion (instead of deposition as before) and the influence of climate change, evaluating the effects of each factor is a prerequisite for studying sediment transport along the coast, the dynamics of erosion and deposition, as well as coastal management at the local area.

This study utilized a numerical model to simulate the coastal current in the Soc Trang area, considering the influential factors of wind and tides on waves. The model employed in this study was developed by [31] and is based on the depth-integrated 2D Reynolds equation in Cartesian coordinates. This model serves as a fundamental tool for assessing and managing coastal protection and risk reduction measures in the region. By implementing a curved coordinate system, the numerical model effectively minimizes errors in areas with complex shorelines. Additionally, the use of an open-source model facilitates the enhancement of monitoring and early warning systems, as it allows for convenient code implementation and further development.

2. Materials and Methods

2.1. Study area

To mitigate the impact of boundary condition errors, the study area was expanded to encompass the sea area stretching from Vung Tau to Ganh Hao in Vietnam. The geographical coordinates of this expanded area range from 302993 to 1085665 east and 797766 to 1328835 north (Figure 1a). This extended study area includes the coastal region of Soc Trang Province along with neighboring provinces. It spans approximately 300 km in length and has a width of approximately 160 km, extending from the shoreline into the sea.

2.2. Data collection

The topographic data used in this study were obtained from the East Sea's topography in 2010, collected and extracted by the Southern Institute of Water Resources Science, Vietnam (SIWRR). A calculating grid was constructed using an orthogonal curved grid format, comprising 130×155 cells. The grid size varied between 150 meters and 300 meters, with dx and dy representing the cell dimensions (Figure 1) [31].

The tidal harmonic constants, including the amplitudes and phases of each tidal constituent, were obtained from the DTU10 Global Tide Model. The data used had a resolution of $0.125^\circ \times 0.125^\circ$ and were extracted specifically for the three open boundaries at sea, namely the left, right, and sea boundaries, as depicted in Figure 1.

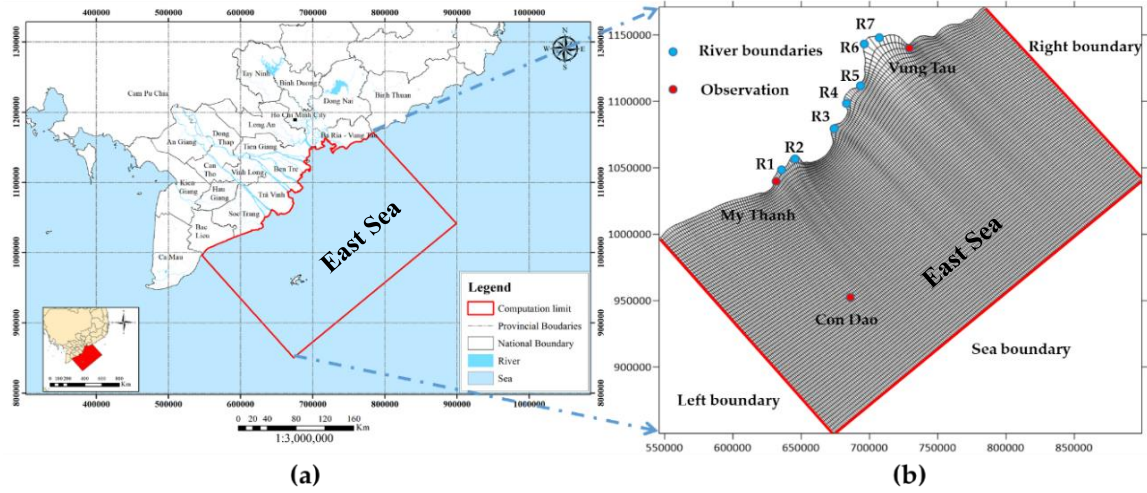


Figure 1. Study area.

To validate the model, hourly water level data from the Vung Tau, Con Dao, and My Thanh stations were collected from the Southern Regional Hydrometeorological Station in 2017. These water level measurements were utilized to verify the accuracy of the model's predictions, in detailed: the water levels from 1:00 am on 01 January 2017 to 1:00 am on February 28, 2017, at Con Dao, from 10:00 am on January 15, 2017, to 10:00 pm on February 14, 2017 at My Thanh station, and from 1:00 a.m. on January 1, 2017, to 10:00 p.m. on February 28, 2017 at Vung Tau station.

Wind data: Wind velocity with a spatial resolution of 0.5 degrees and temporal resolution of 3 hours were collected from <https://cds.climate.copernicus.eu/> from 0:00 am on 01 January 2017 to 23 December 2017.

Wave data: S_{xx} , S_{xy} , S_{yy} stress fields were simulated from the Mike 21SW model from 0:00 am on 01 January 2017 to 23 December 2017, extracted from [32].

2.3. Numerical model description

The governing equations in the curvilinear coordinates (HyCCM Model) are constructed based on the Reynolds equation depth-integrated 2D in Cartesian coordinates [31]. In the 2D model, the vertical velocity component is so small that it is ignored, and the pressure is approximated as the hydrostatic pressure distribution. In previous studies, the nonlinear, Coriolis, friction bed components have been solved in curvilinear coordinate systems. In this study, the two components of wave and wind friction are constructed in a curvilinear coordinate system, as described in Equation 1 [31].

$$\begin{cases} p_\tau + gHJ^{-1}(g_{22}\zeta_\xi - g_{12}\zeta_\eta) = \Psi_1 \\ q_\tau + gHJ^{-1}(g_{11}\zeta_\eta - g_{12}\zeta_\xi) = \Psi_2 \\ JH_\tau + p_\xi + q_\eta = 0 \end{cases} \quad (1)$$

where ξ , η are space coordinates (m).

$$\begin{aligned} \Psi_1 &= \Psi_{a1} + \Psi_{T1} + \Psi_{k1} + \Psi_{S1} + \Psi_{W1} \\ \Psi_2 &= \Psi_{a2} + \Psi_{T2} + \Psi_{k2} + \Psi_{S2} + \Psi_{W2} \end{aligned} \quad (2)$$

where $\tau = t$ is time (s); $p = JUH$ is the ξ component of velocity; $q = JVH$ is the η component of velocity; $H = h + \zeta$; ζ is the fluctuation of the water surface (m); h is the

static depth from the still water surface to the bed (m); Ψ_{a1} and Ψ_{a2} are the ξ and η components of nonlinear [31]; Ψ_{r1} , and Ψ_{r2} are the ξ and η components of friction bed [31]; Ψ_{k1} , and Ψ_{k2} are the ξ and η components of Coriolis [31]; Ψ_{s1} , and Ψ_{s2} , the ξ and η components of wind friction, are calculated as Equations 4-5.

$$\Psi_{S1} = \left[\frac{1}{\rho} C_{10} \rho_a |W| (W_x y_\eta - W_y x_\eta) \right] \quad (4)$$

$$\Psi_{S2} = \left[\frac{1}{\rho} C_{10} \rho_a |W| (W_x x_\xi - W_y y_\xi) \right] \quad (5)$$

$$\text{with } C_{10} = (0.75 + 0.067|W|) \cdot 10^{-3} \quad (6)$$

where W is wind velocity (m/s); ρ_a is the density of air above the sea surface [kg/m^3]; W_x and W_y are the x and y components of wind velocity (m/s), respectively; Ψ_{w1} , and Ψ_{w2} , the ξ and η components of wave friction, are calculated as Equation 7 and Equation 8.

$$\Psi_{W1} = - \left[\frac{I^{-1}}{\rho} (S_{1\xi}(y_\eta y_\eta - y_\eta x_\eta) + S_{1\eta}(y_\xi x_\eta - y_\xi y_\eta) + S_{3\eta}(x_\xi y_\eta - x_\xi x_\eta) + S_{3\xi}(x_\eta x_\eta - x_\eta y_\eta) + (S_{2\xi} g_{22} - S_{2\eta} g_{12})) \right] \quad (7)$$

$$\Psi_{W2} = - \left[\frac{I^{-1}}{\rho} (S_{1\xi}(y_\eta x_\xi - y_\eta y_\xi) + S_{1\eta}(y_\xi y_\xi - y_\xi x_\xi) + S_{3\eta}(x_\xi x_\xi - x_\xi y_\xi) + S_{3\xi}(x_\eta y_\xi - x_\eta x_\xi) + (S_{2\eta} g_{11} - S_{2\xi} g_{12})) \right] \quad (8)$$

$S_1 = S_{xx}$; $S_2 = S_{xy} = S_{yx}$; $S_3 = S_{yy}$ are the x and y components of effective shear stress.

U and V are defined as the ‘‘contravariant’’ base vectors of the curvilinear coordinate system.

The system of Eq. 1 is solved using the alternating direction implicit (ADI) method on the C-Arakawa grid. The mesh nodes are located on the boundary where the velocity component is perpendicular to the boundary. In the algorithm, the water level is simulated using the implicit diagram, employing the semi-implicit ‘‘gradient’’ method. On the other hand, the nonlinear component is solved using an explicit diagram. This combination of implicit and explicit schemes helps in efficiently and accurately modeling the water level and accounting for the nonlinearities in the system [31].

2.4. Model setup

Open boundaries

Water level: water level ζ of 8 tidal constitutions K_1 , O_1 , P_1 , Q_1 , M_2 , S_2 , N_2 and K_2 at three open boundaries at sea (left, right and sea boundaries as Figure 1) are calculated from sigma (σ), amplitude (A), phase (g^0) and period (t), as illustrated in Equation 9:

$$\zeta = A \times \cos(\sigma t - g^0) \quad (9)$$

Sigma (σ) and period (t) are defined in [31], while the amplitude and phase of each tidal constitution are extracted from the DTU10 Global Tide Model at three open boundaries at sea.

River boundaries in estuaries (R_1 , R_2 , R_3 , R_4 , R_5 , R_6 , and R_7 as Figure 1) are discharged and extracted from [33–34].

The stress fields S_{xx} , S_{xy} , and S_{yy} in 2017 are simulated from the Mike 21SW model and extracted from [32].

Wind data: Wind velocity with a resolution of 0.5 degrees, W_x , W_y wind data are obtained from there-analyzed wind data of <https://cds.climate.copernicus.eu/> in 2017.

Land boundary: $u_n = 0$, where n stands for the normal direction.

Initial conditions: the velocity components p and q are zero, and sea level is zero.

The scenarios: four scenarios are simulated in the study:

Cases with wind induced current: these cases simulate only the flow under the influence of wind (use only wind boundaries).

Cases with wave induced current: these cases simulate only the flow under the influence of waves (use only wave boundaries).

Cases with tidal currents: these cases simulate only the flow under the influence of tidal current (use only tidal boundaries).

Coastal current: these cases simulate the flow under the influence of wind, waves, river flow and tidal currents.

The flow chart is illustrated as Figure 2.

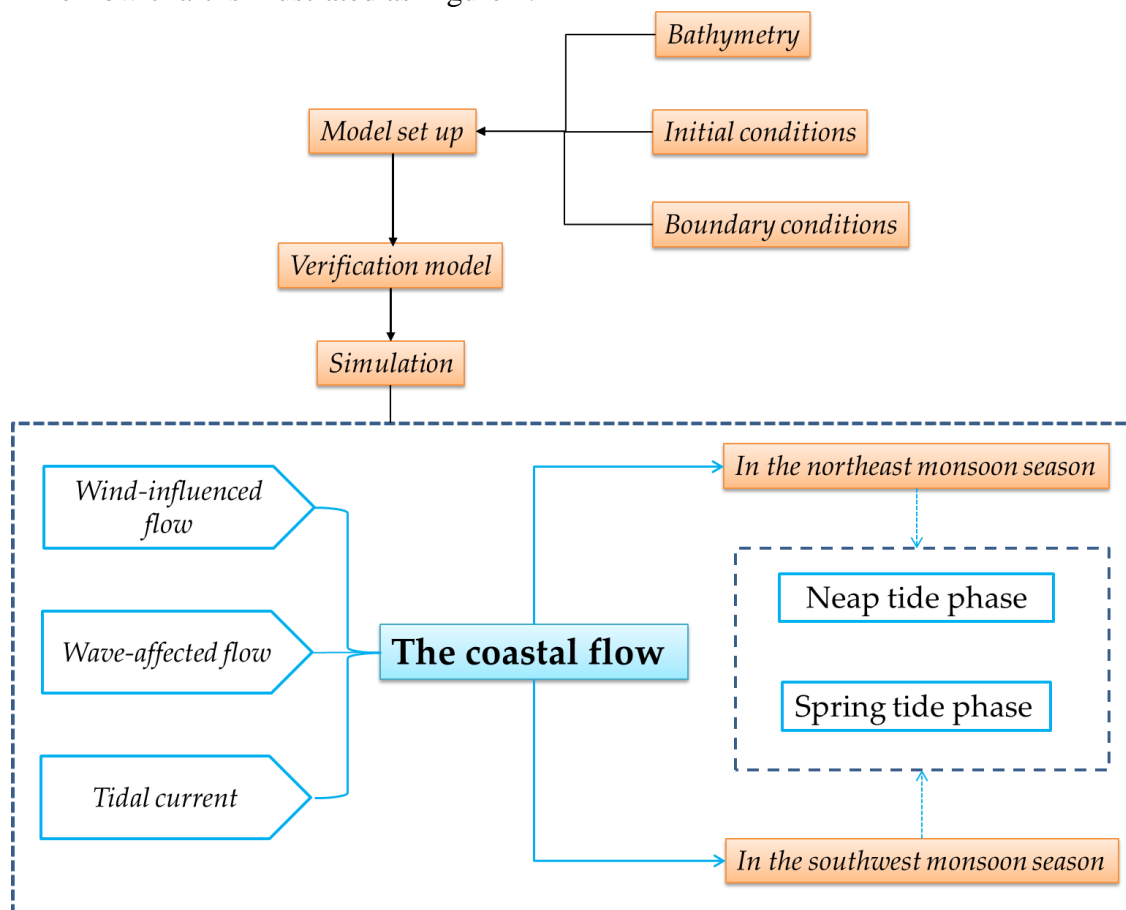


Figure 2. Flow chart of study structure.

2.5. Evaluation criteria

In this study, the Nash-Sutcliffe efficiency coefficient (NSE), the coefficient of determination (R^2) and root mean squared error (RMSE) are required to measure model performance.

The Nash-Sutcliffe efficiency coefficient (NSE)

The Nash-Sutcliffe efficiency coefficient (NSE) ranges between $-\infty$ and 1. $NSE = 1$ indicates a perfect match between the observed and predicted results [35]. NSE is computed as shown in Equation 1:

$$NSE = 1 - \frac{\sum_{i=1}^n (O_i - P_i)^2}{\sum_{i=1}^n (O_i - \bar{O})^2} \quad (10)$$

where O_i is the i^{th} observation for the constituent being evaluated; P_i is the i^{th} simulated value for the constituent being evaluated; \bar{O} is the mean of observed data for the constituent being evaluated; and n is the total number of observations.

The coefficient of determination (R^2)

For the coefficient of determination, R^2 ranges between 0 and 1 and describes the proportion of the variance in the measured data, with higher values indicating less error variance [36]. R^2 is computed as shown in Equation 11:

$$R^2 = \left[\frac{\sum_{i=1}^n (O_i - \bar{O})(P_i - \bar{P})}{\sqrt{\sum_{i=1}^n (O_i - \bar{O})^2 \sum_{i=1}^n (P_i - \bar{P})^2}} \right]^2 \quad (11)$$

where O_i is the i^{th} observation for the constituent being evaluated; P_i is the i^{th} simulated value for the constituent being evaluated; \bar{O} is the mean of observed data for the constituent being evaluated; \bar{P} is the mean of simulation data for the constituent being evaluated; and n is the total number of observations.

Root mean squared error (RMSE)

RMSE values smaller than 0.05 are considered a good fit, values from 0.05 to 0.08 are considered a fair model fit, and values greater than 0.10 are considered a poor fit [38].

$$RMSE = \sqrt{\frac{1}{n} \sum_{i=1}^n (P_i - O_i)^2} \quad (12)$$

where O_i is the i^{th} observation for the constituent being evaluated; P_i is the i^{th} simulated value for the constituent being evaluated; and n is the total number of observations.

3. Results

3.1. Model verification

In the area, the water levels at Con Dao from 1:00 am on 01 January 2017 to 1:00 am on February 28, 2017, at My Thanh station from 10:00 am on January 15, 2017, to 10:00 pm on February 14, 2017, and at Vung Tau station from 1:00 a.m. on January 1, 2017, to 10:00 p.m. on February 28, 2017, are used to verify the model. Three criteria for model performance evaluation include NSE, R^2 and RMSE.

The water level simulations at the three stations show a high agreement between the observed and simulated data in terms of phase and amplitude. The water level comparison between the observations and simulations at Con Dao is better than the results at the My Thanh and Vung Tau stations, with $R^2 = 0.85$, $NSE = 0.83$ and $RMSE = 0.011$ (Figure 3a). While the comparison result in My Thanh is a fair model fit, with $R^2 = 0.78$, $NSE = 0.65$ and $RMSE = 0.053$ (Figure 3b), these values in Vung Tau are lower, at $R^2 = 0.73$, $NSE = 0.63$ and $RMSE = 0.061$ (Figure 3c). The lower water level simulation compared to observations may be caused by the baroclinic effects that were not set up in the model.

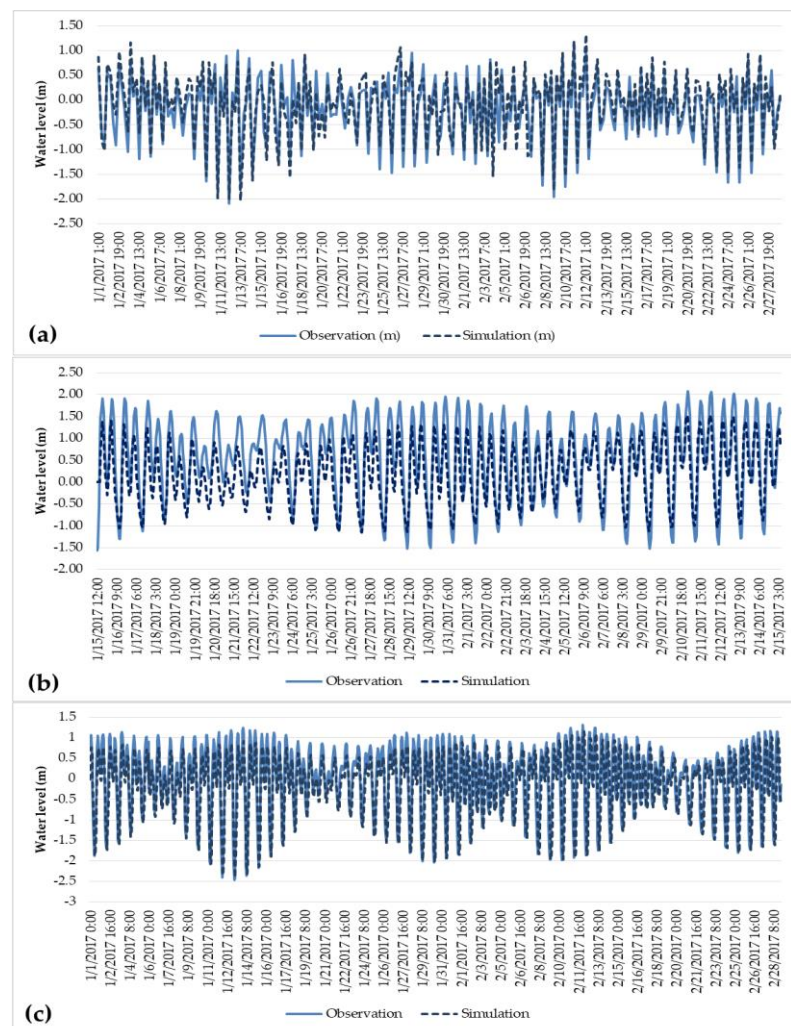


Figure 3. Water level comparison between observation and simulation at Con Dao (a), My Thanh (b) and Vung Tau (c).

The discrepancy in amplitude can be attributed to the water level data obtained from the model for the eight tidal constituents K_1 , O_1 , P_1 , Q_1 , M_2 , S_2 , N_2 and K_2 . While there is a difference in amplitude between the model's data and the observed data, the phase of the water level demonstrates strong consistency. This indicates that these eight tidal constituents exert significant influence in the study area, despite the slight variation in their amplitudes.

After model verification, the roughness coefficient exhibits variability with depth, ranging from 0.026 to 0.058 ($m^{1/3}/s$) as illustrated in Figure 4. The roughness coefficient serves as a measure of the resistance to flow caused by the irregularities of the channel bed and banks. In this case, the coefficient values demonstrate a range of roughness characteristics across different depths within the study area.

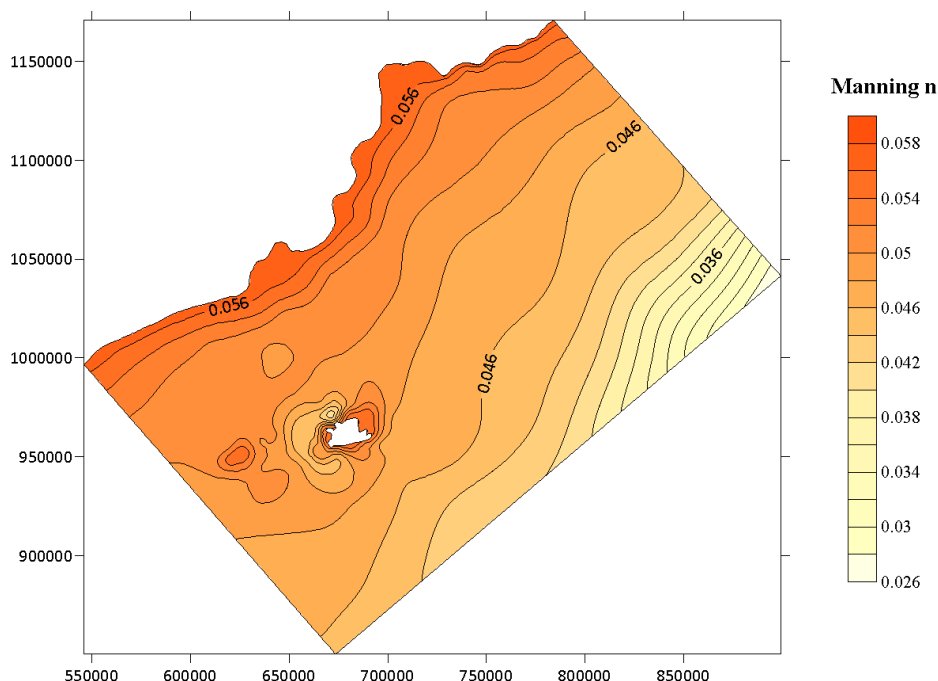


Figure 4. The roughness coefficient map.

3.2. Simulation results of the seasonal flow of the northeast and southwest monsoons

3.2.1. Case with wind induced current

During the northeast monsoon season (November to early March 2017), the simulation results indicate the presence of wind-induced current along the coast, predominantly flowing in a northeast direction. The current velocity in the Soc Trang coastal area is relatively higher and larger compared to other areas, reaching approximately 2.5 cm/s. In contrast, the near-shore area experiences lower current velocities due to the influence of topography and increased bottom friction.

In the Hau Estuaries area, the influence of the northeast wind on the flow is minimal due to the small size and low-lying nature of these areas. The flow velocity in area (a) (Dinh An Estuary) ranges from approximately 0.45 to 0.85 cm/s, while in area (b) (Tran De Estuary), it varies from 0.46 to 0.94 cm/s. Comparatively, the near-shore area (c) exhibits the highest flow velocities among the three areas, ranging from 1.22 to 1.64 cm/s. Additionally, the water level fluctuations in the area gradually increase in the direction of the wind.

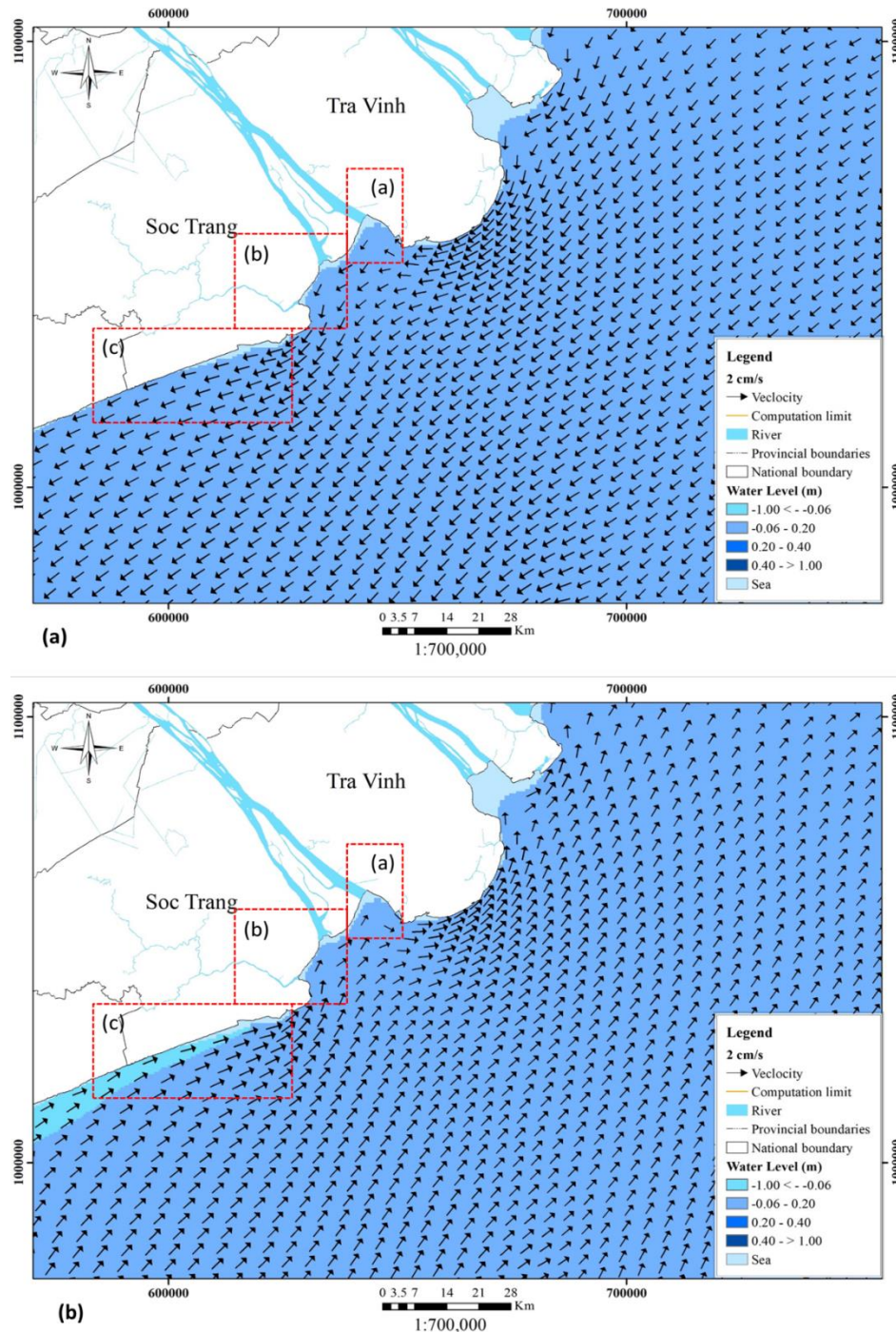


Figure 5. (a) Simulation results of wind induced current in the northeast monsoon season at 15:00 on 25 February 2017; (b) Simulation results of wind induced current in the southwest monsoon season at 9:00 on 26 September 2017.

During the southwest monsoon season (June to early October 2017), the simulation results show a wind-induced current in the study area flowing along the shore in a southwest direction (Figure 5b). The overall flow velocity in the region is relatively small compared to the northeast monsoon season. In the Soc Trang coastal area, the current flow velocity is approximately 2 cm/s (Figure 5b), while in the coastal area, it is slightly smaller.

In the estuary area, the influence of the southwest wind is limited. The flow velocity in area (a) ranges from approximately 0.4 to 0.74 cm/s, in area (b) from 0.42 to 0.82 cm/s, and in area (c) from 1.1 to 1.53 cm/s (Figure 5b). These velocities indicate relatively lower flow rates compared to the coastal and near-shore areas.

3.2.2. Case with wave induced current

The simulation results show the presence of wave-induced currents along the shore in the northeast direction. These currents are formed in the breaking wave zone, where the waves approaching the coastal area undergo dumping and uneven distribution due to shallow water depths and inhomogeneous bottom topography (with water depth being only approximately 1.3 times the wave height). This uneven distribution of waves creates different wave stress fields, and when a wave breaks, the wave energy transforms into a force that moves the water mass, generating shoreline currents.

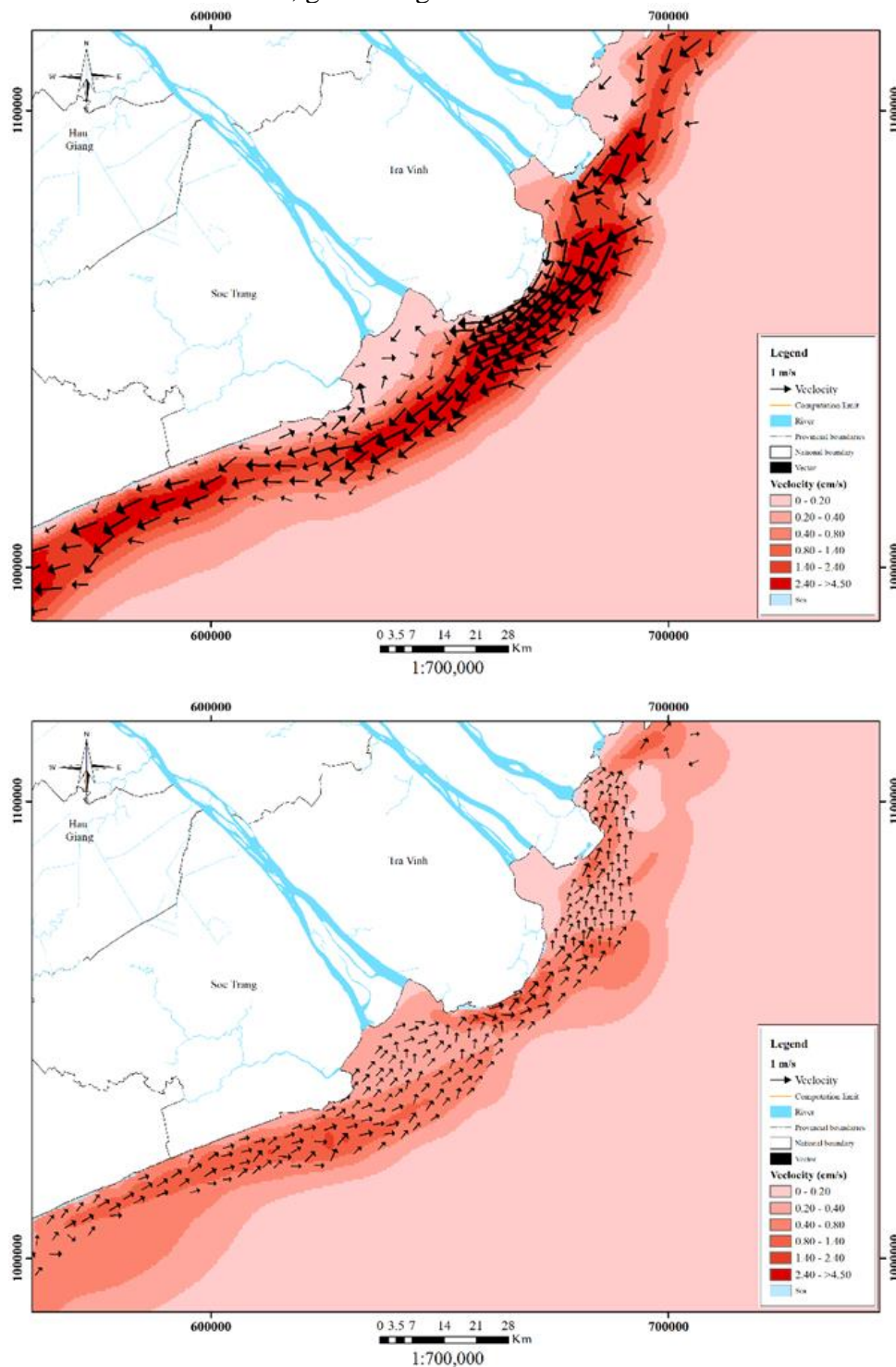


Figure 6. (a) Simulation results of wave induced current in the northeast monsoon season at 15:00 on 25 February 2017; (b) Simulation results of wave effects in the southwest monsoon season at 9:00 on 26 September 2017.

The wave induced current, although relatively small compared to other factors, plays a role in the distribution of suspended sediment in the area. When considering only the flow influenced by waves, the wave-induced current has a width of approximately 6-7 m parallel to the shoreline, primarily located in the breaking wave zone. Specifically, around Con Dao, the width of the wave-induced current is only 3-4 m. The maximum velocity in the near-shore area is around 3.2-5 cm/s in area (c). However, the velocity in the Hau River estuary is significantly smaller. In the Dinh An Estuary (area (a)), the velocity ranges from 0.75-1.5 cm/s, while in the Tran De Estuary (area (b)), it is slightly higher, ranging from 0.78-1.9 cm/s (Figure 6a). The narrow topography and large bottom friction in the river mouth areas minimize the influence of waves on the flow dynamics.

During the southwest monsoon season (July to early October 2017), the simulation results show that the wave-induced current in the area primarily flows in the southwest direction. However, the wave-induced current in the southwest monsoon season is generally weaker than that in the northeast monsoon season.

At the mouth of the Hau River, there are vortices with insignificant velocity, approximately 0.2 cm/s in area A. The maximum velocity of the wave-induced current is only 3.6 cm/s in the coastal section of Soc Trang Province (area (c)). Compared to the northeast monsoon season, the coastal current has a lower velocity during the southwest monsoon (Figure 6b). There is no significant difference in the simulation results of the flow velocity in the Dinh An and Tran De estuaries, with ranges of 0.5-1.2 cm/s and 0.52-1.3 cm/s, respectively (in areas (a) and (b) in Figure 6b).

Overall, the simulation results demonstrate that the offshore velocity is small, but as the waves approach the breaking wave area, the velocity increases. The maximum velocity is reached at the breaking point and then decreases abruptly as the waves approach the shore. The wave direction in the area, influenced by the monsoon seasons, plays a significant role. During the northeast monsoon, the wave direction is northeasterly, while during the southwest monsoon, it is southwesterly. These directional changes are consistent with previous studies on the South China Sea area [24, 39–41]. To fully consider the contribution of coastal currents to regional flows, it is essential to consider the overall influence of wind-wave factors, river currents, and tidal currents.

3.2.3. Case with tidal currents

In the study area, the tidal currents generally follow the direction of tidal currents in the East Sea. The dominant tide in the area is irregular semidiurnal, and the tidal range, which is the difference between high tide and low tide, ranges from 2 m to 4 m during the day [24, 42]. The flow velocities during the spring tide and neap tide phases were extracted at 13:00 and 19:00 on 15 February 2017, respectively.

During the spring tide phase (Figure 7a), the tidal current flows in the northeast direction from the East Sea towards the estuaries. The highest velocity, reaching nearly 1 m/s, is observed at the river mouth, while the overall velocity in the region is lower. The tidal current velocity close to the shore is negligible. In the Dinh An estuary (area (a)), the tidal current velocities range from 0.54 m/s to 0.96 m/s, while in the Tran De estuary (area (b)), they range from 0.4 m/s to 0.92 m/s. Comparatively, the study findings differ from [23], which analyzed the mean water surface slope and showed higher velocities in the Dinh An channel compared to the Tran De channel.

During the neap tide phase (Figure 7b), the difference between the tidal current velocities in the estuary and coastal area becomes more pronounced compared to the spring tide phase. The tidal current velocity in the Dinh An estuary ranges from 0.44 m/s to 0.92 m/s, and in the Tran De estuary, it ranges from 0.35 m/s to 0.9 m/s, which is approximately triple the velocity observed in the coastal area (0.2 m/s).

These results indicate that tidal current velocities vary with tidal phases, with higher velocities during spring tide and lower velocities during neap tide. The estuaries experience stronger tidal currents compared to the coastal area, with the Dinh An estuary generally exhibiting higher velocities than the Tran De estuary.

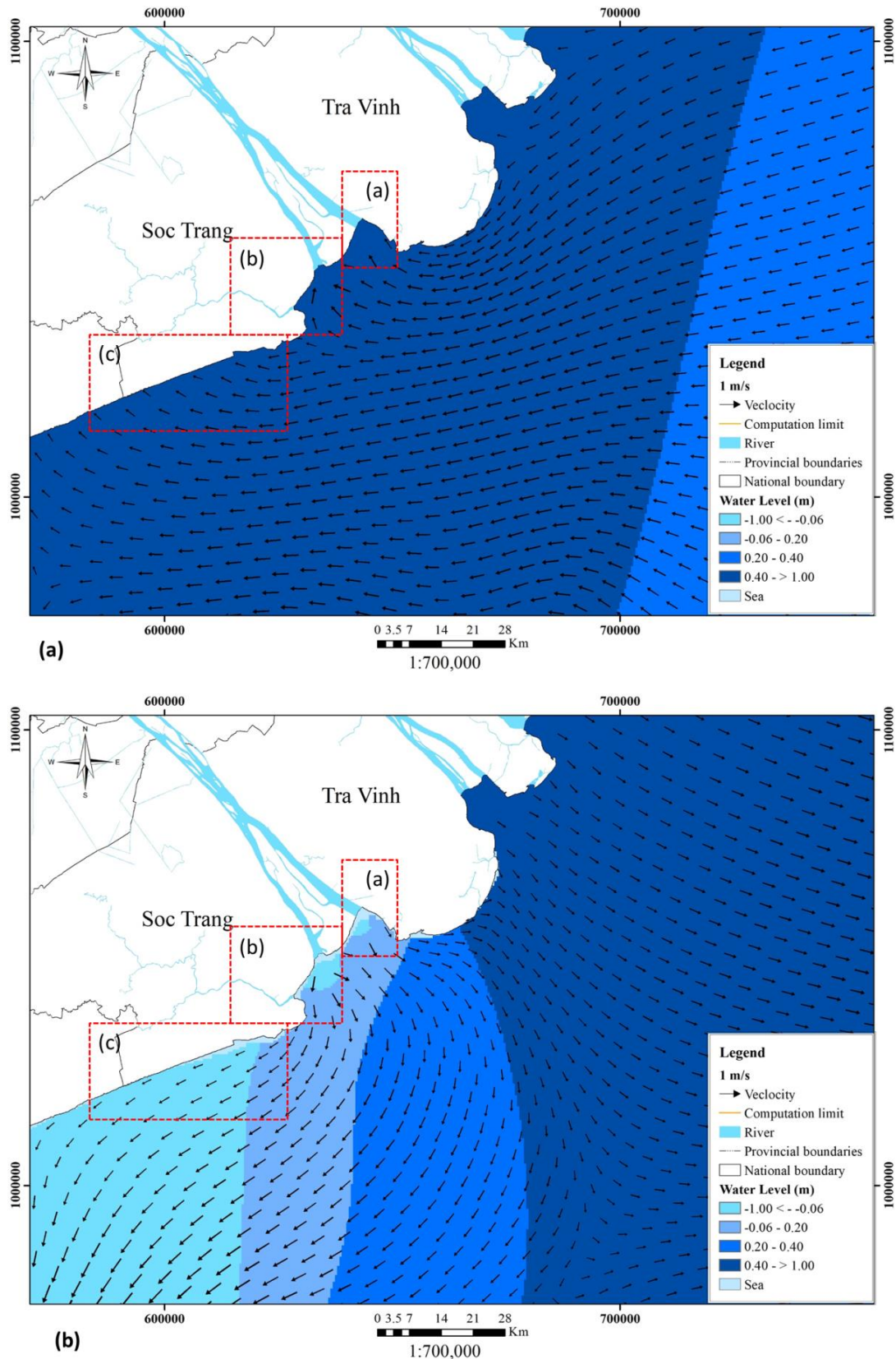


Figure 7. (a) Simulation results of the tidal current at spring tide at 13:00 on 15 February 2017; (b) Simulation results of the tidal current at neap tide at 19:00 on 15 February 2017.

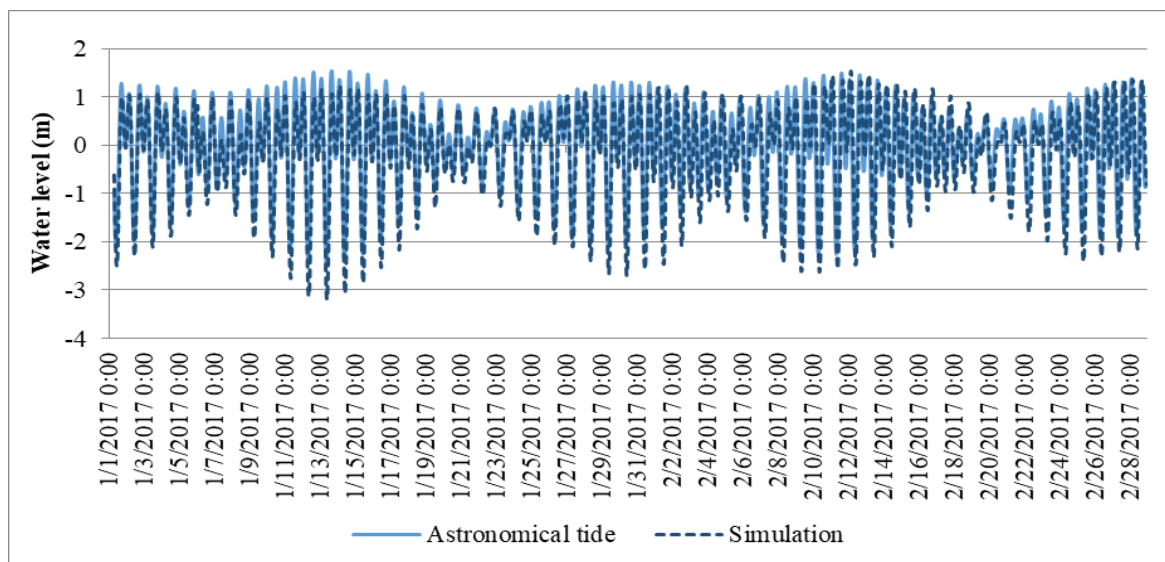


Figure 8. Water level comparison between astronomical tide and simulation at Vung Tau.

When comparing the results with the astronomical tide forecast at Vung Tau, considering only the influence of tides, the findings show a close match between the astronomical tide and the calculated results from the model, with $R^2 = 0.93$, $NSE = 0.91$ and $RMSE = 0.008$ (Figure 8). The calculation of these results is explained by the fact that the input data of the model include the extraction of the amplitude and phase of each tidal component from the DTU10 Global Tide Model.

3.2.4. Coastal current

During the northeast monsoon season, the coastal current in the study area is primarily influenced by tidal currents. The tidal currents flow from the northeast, which is the same direction as the wave induced current. This alignment leads to an increase in the coastal current during both the spring tide and neap tide phases.

During the spring tide phase (Figure 9a), the coastal current experiences an approximate increase of 3-5%. Similarly, during the neap tide phase (Figure 9b), the coastal current sees an increase of approximately 2-5%. These increases in coastal current are attributed to the combined effects of tidal currents and wave induced currents. The influence of wind on the study area is considered insignificant in comparison.

The maximum velocity recorded in the Dinh An Estuary during the spring tide phase is 1.08 m/s, and during the neap tide phase, it is 1.12 m/s (areas (a) and (b) in Figure 9a and 9b). In the Tran De Estuary, the maximum velocity is slightly lower, measuring 0.92 m/s during the spring tide phase and 0.94 m/s during the neap tide phase (areas (a) and (b) in Figures 9a, 9b).

Therefore, in the northeast monsoon season, the coastal current in the study area is primarily driven by tidal currents, with some contribution from wave induced currents, while wind has minimal influence on the coastal current dynamics. The velocity of the neap tide in these estuaries is higher than that of the spring tide due to river discharge. The discharge in the Dinh An Estuary is 33.48 m³/s in the spring tide and is -33.79 m³/s in the neap tide, while that in the Tran De Estuary is 20.63 m³/s in the spring tide and is -21.85 m³/s in the neap tide (Symbol “-” means flow direction in the neap tide).

Similarly, during the southwest monsoon season, the tidal current that flows from northeast to southwest has the opposite direction to the wave induced current (from southwest to northeast), leading to a decrease in the combined current at spring tide (3-4%) (Figure 9c) and at neap tide (3-4.5%) (Figure 9d).

During the spring tide phase, the tidal current from the East Sea (belong to South China Sea) flows toward the Mekong estuaries, creating two main tidal trends: tidal currents from the southwest and tidal currents from the northeast. When reaching the mouth of the Hau River, the northeast tidal current is phased earlier, resulting in a tendency for the flow to have a northeast direction when the tide rises in the southwest monsoon season. The eddies in the Hau estuary are caused by the interference of tidal currents and currents in the river. The maximum velocity in the Dinh An Estuary is 1.1 m/s in the spring tide phase, which is higher than that in Tran De Estuary, at 0.9 m/s (34.59 m³/s of discharge in Dinh An Estuary and 20.56 m³/s of discharge in Tran De Estuary) (Figure 9c).

During the neap tide phase, the value of coastal current velocity at locations in the southwest monsoon is mostly smaller than the flow in the northeast monsoon at the spring tide. However, there are some locations near the mouth of the Dinh An River where the value of the flow in the southwest monsoon is higher; during this season, the flood water from the river is greater, with peaks in late summer (August-September) [39]. The maximum velocity in the Dinh An Estuary is 1.14 m/s, which is higher than that in the Tran De Estuary, at 0.94 m/s (-34.76 m³/s of discharge in the Dinh An Estuary and -21.83 m³/s of discharge in the Tran De Estuary) (Figure 9d).

The coastal current results from the dominance of the wind, wave, river flow and tidal currents of the northeast monsoon, as the flow in the southwest monsoon is much weaker than that in the northeast monsoon. In the estuary, the river flow still dominates; the discharge from upstream greatly affects its flow velocity.

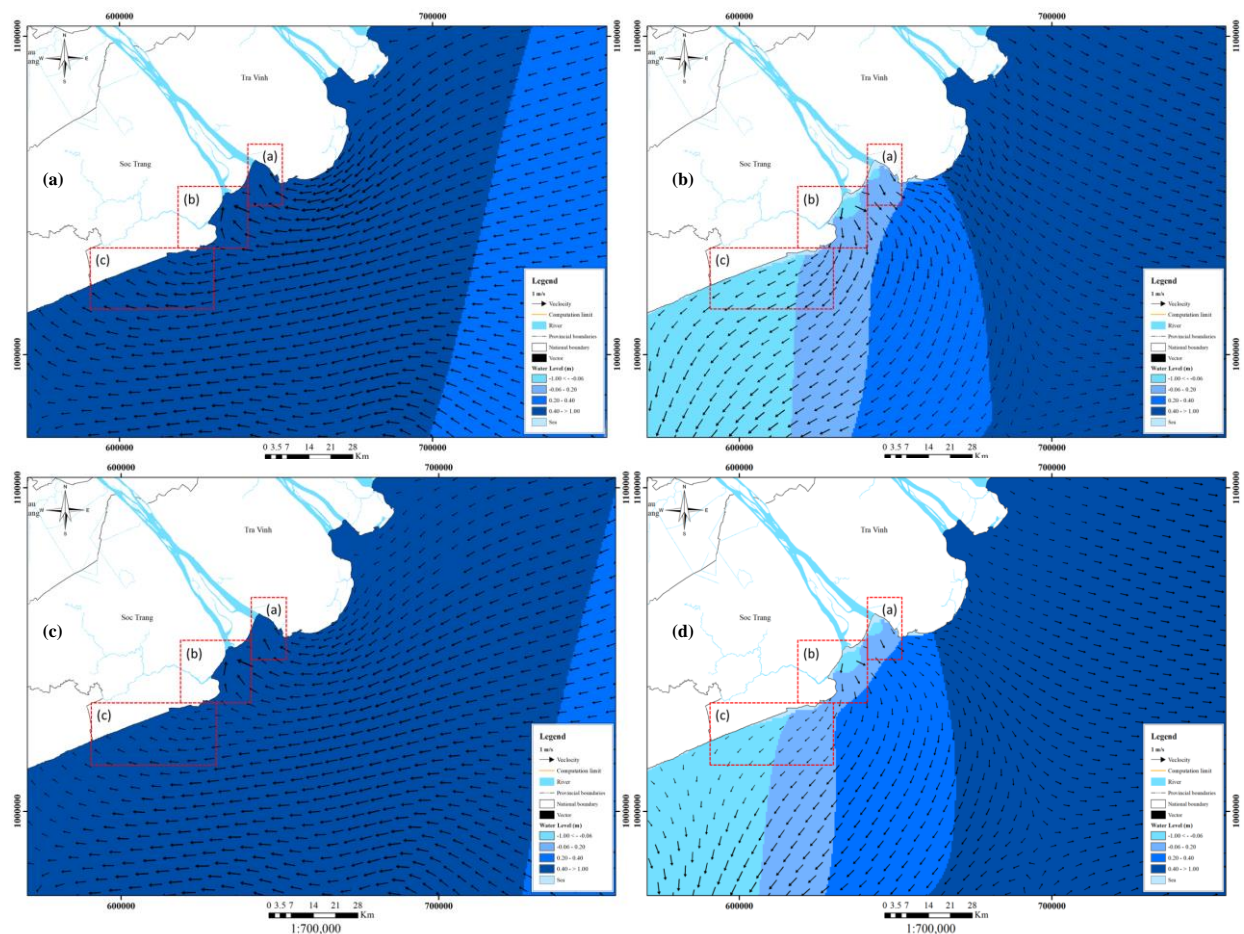


Figure 9. Simulation results of the coastal current in: (a) the northeast monsoon season at spring tide phase at 13:00 on 15 February 2017; (b) the northeast monsoon season at neap tide phase at 19:00 on 15 February 2017; (c) the southwest monsoon season at spring tide phase at 14:00 on 20 September 2017; (d) the southwest monsoon season at neap tide phase at 20:00 on 20 September 2017.

To compare the influence of wave, wind and tide factors in the study area, three positions S1, S2 and S3 are extracted to consider the velocity value, these three positions are described as in Table 1.

Table 1. The extraction sites.

No	Name	Lattitude	Longitude
1	S1	9°09'05.80"N	105°55'31.87"E
2	S2	9°13'35.21"N	106°09'27.98"E
3	S3	9°25'09.94"N	106°13'19.50"E

According to the statistical results from Figure 10 and Figure 11, because the wave induced current and the wind induced current in the Northeast monsoon has a Southwest - Northeast direction, coinciding with the spring and neap tides during the Northeast monsoon, so the coastal current velocity increases. Meanwhile, because the wave induced current and the wind induced current in the Southwest monsoon have a Northeast-Southwest direction, in contrast with the spring and neap tides during the Southwest monsoon, the flow velocity decreases. The influence of waves and winds deep into the estuary is negligible.

This result is quite similar to the simulation results of currents under the influence of waves and tides in both direction and magnitude in the study of [27].

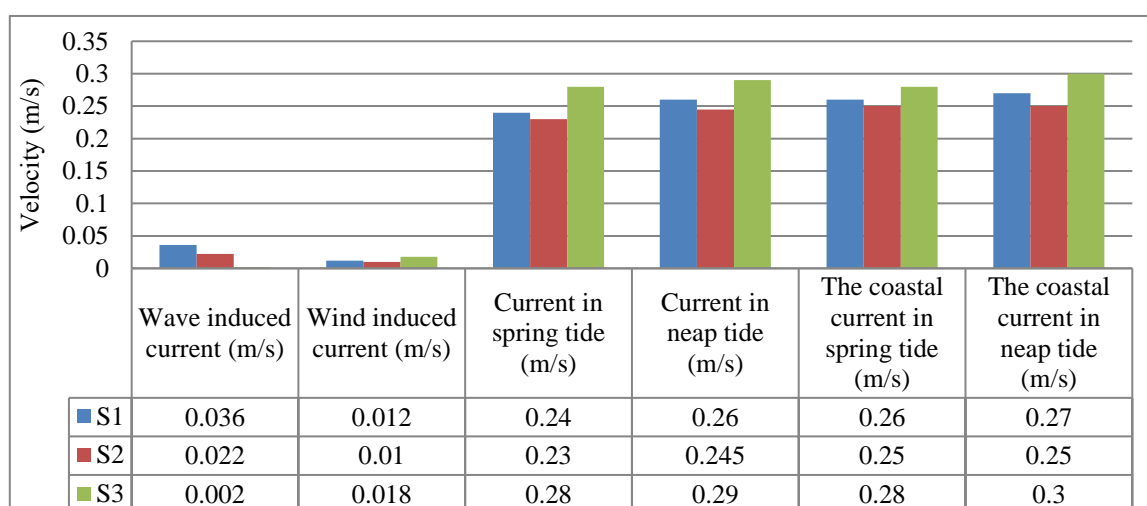


Figure 10. Coastal current velocity of each single element and total flow during the Northeast monsoon season at the extraction sites.

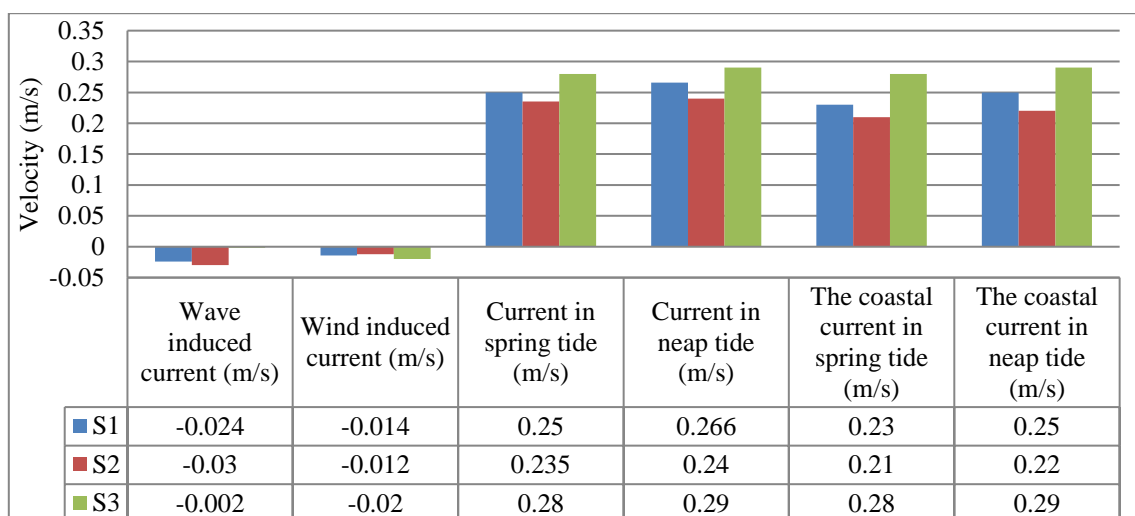


Figure 11. Coastal current velocity of each single element and total flow during the Southwest monsoon season at the extraction sites.

4. Conclusion

The coastal currents in the study area are influenced by various factors, including wind, waves, and tides. During the northeast monsoon season, wind induced currents flow along the coast in the northeast direction, with the highest velocity of 2.5 cm/s observed in the Soc Trang coastal area. In the southwest monsoon season, the wind induced currents flow along the shore in the southwest direction, but with lower velocities compared to the northeast monsoon season. Wave induced currents are also influenced by the wind seasons, flowing from the northeast to the southwest and into the West Sea during the northeast monsoon, and from the southwest to the northeast during the southwest monsoon. The velocities of wave induced currents are generally higher in the northeast monsoon season. However, tidal currents dominate the coastal currents, with significantly higher velocities than wind and wave induced currents. During the spring tide phase, tidal currents reach their maximum velocities, nearly 1 m/s at the river mouth, while remaining relatively smaller in the overall region. In the Dinh An estuary, tidal current velocities range from 0.54 to 0.96 m/s, and in the Tran De estuary, they range from 0.4 to 0.92 m/s. During the neap tide phase, the velocity difference between the river mouth and surrounding areas is even more pronounced. Tidal currents close to the shore have negligible velocities.

Regarding the coastal current, in the northeast monsoon season, the tidal currents from the northeast-southwest are in the same direction as the wave induced current, leading to an increase in the coastal current during spring tide (3-5%) and at neap tide (2-5%). In the southwest monsoon season, the direction is the opposite for tidal current and wave induced current; as a result, the velocities of the coastal current decrease at high tide (3-4%) and low tide (3-4.5%). The influence of winds deep in the estuary (Tran De and Dinh An estuaries) is negligible because these areas are small and low-lying, which reduces the influence of wind on the flow.

However, this study has not yet assessed the influence of wave induced currents on sediment transport along the coast, which is also a research direction for the future. In this study, some uncertainties that may affect the calculated results are the boundary conditions at the sea, which only consider the eight major tidal constituents.

Author Contributions: Conceptualization, T.T.K., N.T.B.; methodology, T.T.K., N.V.P., N.T.B., N.K.P.; software, T.T.K., N.D.Q.H., P.T.M.D., P.A.T.; validation, P.T.M.D.; formal analysis, T.T.K., P.T.M.D., N.D.Q.H.; investigation, N.T.B., N.K.P.; resources, N.T.B.; data curation, N.D.Q.H., N.T.B.; writing—original draft preparation, T.T.K., N.T.B.; writing—review and editing, T.T.K., N.T.B.; visualization, N.V.P., N.D.Q.H.; supervision, N.K.P., N.T.B.; project administration, N.K.P.; funding acquisition, N.K.P.

Acknowledgments: We would like to thank Ho Chi Minh City University of Technology (HCMUT), VNU–HCM for their donations of time and facilities for this study.

Conflicts of Interest: The authors declare no conflict of interest.

References

1. Tran, D.A.; Hoang, L.P.; Bui, M.D.; Rutschmann, P. Simulating future flows and salinity intrusion using combined one-and two-dimensional hydrodynamic modelling the case of Hau River, Vietnamese Mekong delta. *Water* **2018**, *10*(7), 897.
2. Stansby, P.K. Coastal hydrodynamics-present and future. *J. Hydraul. Res.* **2013**, *51*(4), 341–350.
3. Chang, S.W. et al. Does sea-level rise have an impact on saltwater intrusion? *Adv. Water. Resour.* **2011**, *34*(10), 1283–1291.
4. Galland, J.; Goutal, C.N.; Hervouet, J.M. TELEMAC: A new numerical model for solving shallow water equations. *Adv. Water. Resour.* **1991**, *14*(3), 138–148.
5. Hervouet, J.M. TELEMAC modelling system: an overview. *Hydrol. Processes* **2000**, *14*(13), 2209–2210.

6. Zangiabadi, E. et al. Computational fluid dynamics and visualisation of coastal flows in tidal channels supporting ocean energy development. *Energies* **2015**, 8(6), 5997–6012.
7. de Saint-Venant, B.A.J.C. Théorie du Mouvement Non Permanent des Eaux, avec Application aux Crues de Rivières et à l'Introduction des Marées dans leur Lit. Comptes Rendus des séances de l'Académie des Sciences, 1871, pp. 147–154.
8. Castro-Orgaz, O.; Hager, W.H. Shallow water hydraulics. *Springer*, **2019**.
9. Ersoy, M.; Lakkis, O.; Townsend, P. A Saint-Venant model for overland flows with precipitation and recharge. *Math. Comput. Appl.* **2020**, 26(1), 1.
10. Jia, Y.; Wang, S.S. Numerical model for channel flow and morphological change studies. *J. Hydraul. Eng.* **1999**, 125(9), 924–933.
11. Jia, Y.; Wang, S.S. CCHE2D: Two-dimensional hydrodynamic and sediment transport model for unsteady open channel flows over loose bed. National Center for Computational Hydroscience Engineering, Technical Report No. NCCHE-TR-1, 2001.
12. Thakur, B. et al. Exploring CCHE2D and its sediment modelling capabilities. in World Environmental and Water Resources Congress 2018: Hydraulics and Waterways, Water Distribution Systems Analysis, and Smart Water. American Society of Civil Engineers Reston, VA, 2018.
13. Kadam, P.; Sen, D. Flood inundation simulation in Ajoy River using MIKE–FLOOD. *ISH J. Hydraul. Eng.* **2012**, 18(2), 129–141.
14. Nigussie, T.A.; Altunkaynak, A. Modeling the effect of urbanization on flood risk in Ayamama Watershed, Istanbul, Turkey, using the MIKE 21 FM model. *Nat. Hazard.* **2019**, 99(2), 1031–1047.
15. Sarker, S. Essence of MIKE 21C (FDM Numerical Scheme): Application on the River Morphology of Bangladesh. *Open J. Modell. Simul.* **2022**, 10(2), 88–117.
16. Bomers, A.; Schielen, R.M.J.; Hulscher, S.J. The influence of grid shape and grid size on hydraulic river modelling performance. *Environ. Fluid. Mech.* **2019**, 19(5), 1273–1294.
17. Baker, T.J. Discretization of the Navier Stokes equations and mesh induced errors. Mississippi State Univ. Mississippi State, MS (United States): United State, 1996.
18. Liu, X.; Ma, J.; Xu, S.; Wang, B. On the generation of coastline-following grids for ocean models—trade-off between orthogonality and alignment to coastlines. *Ocean. Dyn.* **2017**, 67, 1095–1104.
19. Morianou, G.G.; Kourgialas, N.N.; Karatzas, G.P.; Nikolaidis, N.P. Assessing hydro-morphological changes in Mediterranean stream using curvilinear grid modeling approach-climate change impacts. *Earth. Sci. Inf.* **2018**, 11(2), 205–216.
20. Yousefi, K.; Veron, F. Boundary layer formulations in orthogonal curvilinear coordinates for flow over wind-generated surface waves. *J. Fluid Mech.* **2020**, 888, A11.
21. Truong, Q.C.; Nguyen, T.H.; Tatsumi, K.; Pham, V.T.; Tri, V.P.D. A Land-Use Change Model to Support Land-Use Planning in the Mekong Delta (MEKOLUC). *Land* **2022**, 11(2), 297.
22. Tran, D.A.; Tsujimura, M.; Vo, L.P.; Nguyen, V.T.; Kambuku, D.; Dang, T.D. Hydrogeochemical characteristics of a multi-layered coastal aquifer system in the Mekong Delta, Vietnam. *Environ. Geoche. Health* **2020**, 42(2), 661–680.
23. Xing, F.; Meselhe, E.A.; Allison, M.A.; Weathers III, H.D. Analysis and numerical modeling of the flow and sand dynamics in the lower Song Hau channel, Mekong Delta. *Cont. Shelf Res.* **2017**, 147, 62–77.
24. Tamura, T.; Horaguchi, K.; Saito, Y.; Nguyen, V.L.; Tateishi, M.; Ta, T.K.O.; Nanayama, F.; Watanabe, K. Monsoon-influenced variations in morphology and sediment of a mesotidal beach on the Mekong River delta coast. *Geomorphology* **2010**, 116(1–2), 11–23.
25. Thanh, V.Q. et al. Sediment transport and morphodynamical modeling on the estuaries and coastal zone of the Vietnamese Mekong Delta. *Cont. Shelf. Res.* **2019**, 186, 64–76.

26. Bayrak, M.M.; Marks, D.; Hauser, L.T. Disentangling the concepts of global climate change, adaptation, and human mobility: A political-ecological exploration in Vietnam's Mekong Delta. *Clim. Dev.* **2022**, *14*(10), 1–10.
27. Marchesiello, P.; Nguyen, N.M.; Gratiot, N.; Loisel, H.; Anthony, E.J.; Dinh, C.S.; Nguyen, T.; Almar, R.; Kestenare, E. Erosion of the coastal Mekong delta: Assessing natural against man induced processes. *Cont. Shelf. Res.* **2019**, *181*, 72–89.
28. Thanh, V.Q.; Reyns, J.; Wackerman, C.; Eidam, E.F.; Roelvink, D. Modelling suspended sediment dynamics on the subaqueous delta of the Mekong River. *Cont. Shelf. Res.* **2017**, *147*, 213–230.
29. Nguyen, N.M.; San, D.C.; Nguyen, K.D.; Pham, Q.B.; Gagnon, A.S.; Mai, S.T.; Anh, D.T. Region of freshwater influence (ROFI) and its impact on sediment transport in the lower Mekong Delta coastal zone of Vietnam. *Environ. Monit. Assess.* **2022**, *194*(7), 1–15.
30. Mai, N.P.; Thang, T.D.; Kantoush, S.; Sumi, T.; Binh, D.V.; Trung, L.V. The processes of saltwater intrusion into Hau River. Proceeding of the International Conference on Asian and Pacific Coasts. *APAC 2019*, pp. 1477–1483.
31. Kim, T.T.; Long, N.K.T.; Hong, N.T.T.; Phung, N.K.; Bay, N.T. Mapping the residual tidal ellipse from Vung Tau–Bac Lieu, Viet Nam by using a numerical model in curvilinear coordinate. *VN J. Hydrometeorol.* **2021**, *8*, 50–63.
32. Kim, T.T.; Nguyen, T.T.P.; Hoang, H.K.; Nguyen, T.T.H.; Nguyen, T.N.M.; Phung, D.T.M. Mapping erosion-accretion risk maps in the coastal area of Soc Trang. *VN Sci. Tech. Dev. J.* **2021**, *5*(SI2), SI64–SI74.
33. Kim, T.T.; Bay, N.T.; Ky, P.N.; Nguyen, M.T.T.; Tra, N.N.Q. Bottom morphology in hau estuaries under influences of sediment reduction and climate variation. *VN Sci. Tech. Dev. J.* **2021**, *4*(SI1), SI84–SI94.
34. Thuy, N.T.D. et al. Modelling Accretion and Erosion Processes in the Bassac and Mekong Rivers of the Vietnamese Mekong Delta. Proceeding of the APAC 2019: Proceedings of the 10th International Conference on Asian and Pacific Coasts. Springer, Hanoi, Vietnam, APAC 2019, pp. 1431–1437.
35. Nash, J.E.; Sutcliffe, J.V. River flow forecasting through conceptual models part I—A discussion of principles. *J. Hydrol.* **1970**, *10*(3), 282–290.
36. Moriasi, D.N.; Arnold, J.G.; Van Liew, M.W.; Bingner, R.L.; Harmel, R.D.; Veith, T.L. Model evaluation guidelines for systematic quantification of accuracy in watershed simulations. *Trans ASABE.* **2007**, *50*(3), 885–900.
37. Steiger, J.H. Statistically based tests for the number of common factors. in the annual meeting of the Psychometric Society. Iowa City, IA. 1980.
38. Browne, M.W.; Cudeck, R. Alternative ways of assessing model fit In KA Bollen & JS Long (Eds.), Testing structural equation models. Newbury Park, CA: Sage, **1993**, 136–162.
39. Chen, C.; Lai, Z.; Beardsley, R.C.; Xu, Q.; Lin, H.; Viet, N.T. Current separation and upwelling over the southeast shelf of Vietnam in the South China Sea. *J. Geophys. Res: Oceans* **2012**, *117*(C3), C03033.
40. Shi-Feng, S. Waves in South China Sea, in Oceanology of China Seas. *Oceanology China Seas* **1994**, 135–140.
41. Mirzaei, A.; Tangang, F.; Juneng, L.; Mustapha, M.A.; Husain, M.L.; Akhir, M.F. Wave climate simulation for southern region of the South China Sea. *Ocean Dyn.* **2013**, *63*(8), 961–977.
42. Gugliotta, M.; Saito, Y.; Nguyen, V.L.; Ta, T.K.O.; Nakashima, R.N.; Tamura, T.; Uehara, K.; Katsuki, K.; Yamamoto, S. Process regime, salinity, morphological, and sedimentary trends along the fluvial to marine transition zone of the mixed-energy Mekong River delta, Vietnam. *Cont. Shelf Res.* **2017**, *147*, 7–26.